Article

Not peer-reviewed version

Non-Contact Bearing Fault Diagnostics: Experimental Investigation of Microphones Position and Distance

Emanuele Voltolini , Andrea Toscani * , Enrico Armelloni , Marco Cocconcelli , Lorenzo Fendillo , Elisabetta Manconi

Posted Date: 7 April 2026

doi: 10.20944/preprints202604.0395.v1

Keywords: condition monitoring; rolling bearing; non-contact diagnostic; envelope analysis; microphone; accelerometer; digital acquisition system

 doi:10.20944/preprints202604.0395.v1

Article

Non-Contact Bearing Fault Diagnostics: Experimental Investigation of Microphones Position and Distance

Emanuele Voltolini [1], Andrea Toscani [2,*], Enrico Armelloni [1], Marco Cocconcelli [3], Lorenzo Fendillo [1] and Elisabetta Manconi [1]

[1] Department of Engineering for Industrial Systems and Technologies, University of Parma, 43124 Parma, Italy

[2] Department of Engineering and Architecture, University of Parma, 43124 Parma, Italy

[3] Department of Sciences and Method for Engineering, University of Modena and Reggio Emilia, 42122 Reggio Emilia, Italy

* Correspondence: andrea.toscani@unipr.it; Tel.: +39 0521 906007

Featured Application

The proposed microphone-based diagnostic approach is suitable for non-contact condition monitoring of rolling bearings in industrial environments where the installation of contact sensors is impractical or unsafe. Potential applications include industrial machinery, and retrofit monitoring of existing assets, where optimal microphone placement combined with HFRT-envelope based analysis enables fault detection at a distance.

Abstract

Monitoring the condition of rolling bearings is critical for industrial reliability, yet traditional contact-based accelerometers can be impractical in confined or hazardous environments. This study investigates the use of microphones as a non-invasive diagnostic alternative, focusing on the impact of sensor distance and spatial placement on fault detection sensitivity across various rotational speeds and load conditions. Using an accelerometer mounted directly on the bearing as a benchmark, acoustic data were acquired on a test bench under different speed and load conditions. The experimental setup evaluated three distinct microphones positions and five distances relative to the source to assess spatial influence. Analysis was conducted comparing scalar indicators, such as Root Mean Square (RMS), Kurtosis and Crest Factor (CF) values, with advanced diagnostic techniques, specifically the High-Frequency Resonance Technique (HFRT) for envelope spectrum extraction. Results indicate that while the signal-to-noise ratio (SNR) predictably decreases with distance, diagnostic performance is significantly compromised by acoustic shielding effects caused by bearing housing. Moreover, while simple statistical factors (RMS, Kurtosis, CF) show limited reliability across varying distances and noise floors, HFRT-based envelope analysis yields robust fault identification even at the maximum sensor distance. The study concludes that optimal microphone placement is essential for reliable remote monitoring. Particularly, these findings suggest that a preliminary spatial characterization of the acoustic field can significantly enhance the effectiveness of non-contact diagnostic systems in industrial applications.

Keywords: condition monitoring; rolling bearing; non-contact diagnostic; envelope analysis; microphone; accelerometer; digital acquisition system

1. Introduction

Monitoring rolling bearing condition [1,2] is a fundamental pillar of industrial reliability and predictive maintenance strategies [3–7]. Traditionally, contact-based vibration monitoring using piezoelectric accelerometers has been the gold standard for defect detection due to its high sensitivity

 doi:10.20944/preprints202604.0395.v1

and direct connection to the source of mechanical excitation [8–10]. However, in some real-world industrial scenarios, such as machinery operating in hazardous environments, confined spaces or high-temperature applications, mounting sensors directly on the bearing housing is often impractical or limited by accessibility constraints [11]. As a result, there is a growing demand for non-invasive, remote diagnostic alternatives that can provide reliable health status information without physical contact [12,13].

Acoustic monitoring using measurement and ultrasonic microphones has established itself as a promising solution for non-contact diagnostics [14–19]. Although microphones offer ease of installation and the ability to monitor multiple components simultaneously, their effectiveness is often hampered by the inherent difficulties of the acoustic transmission path. Key issues include the rapid attenuation of the SNR with distance and the presence of fluid-dynamic noise generated by rotating shafts. In addition, the complex geometry of bearing housings can act as an acoustic screen, significantly distorting or shielding the fault signal before it reaches the sensor.

The purpose of this study is to systematically investigate the impact of microphone placement and distance on the sensitivity of bearing fault detection at various operating speeds and load conditions. Using a housing-mounted accelerometer as a reference point, an experimental campaign was conducted to evaluate the diagnostic performance of a microphone in three different positions and at five discrete distances. The study goes beyond simple scalar indicators, such as RMS, Kurtosis and CF analysis, by implementing the HFRT for envelope spectrum extraction, a method specifically designed to isolate impulsive fault signatures by targeting high-frequency structural resonances [20–23].

Compared to prior studies that mainly focus on denoising, decomposition, or multimodal classification [24–26], this work isolates the geometric acquisition problem by experimentally quantifying how micro-phone spacing and azimuthal placement affect the recoverability of BPFO signatures using conventional HFRT processing.

While the present work focuses on signal processing and feature extraction under constant speed conditions, the underlying dynamic mechanisms — explored in the literature [27,28] —remain beyond the scope of this investigation.

The main conclusions reveal that, while scalar energy indicators are strongly influenced by background interference and low-frequency fluid-dynamic noise, the envelope spectrum ratio remains a reliable diagnostic indicator even at extended distances. More importantly, the results demonstrate that sensor placement is as critical as distance; specifically, the bearing housing acts as a physical barrier, necessitating strategic microphone positioning to mitigate acoustic shielding effects and ensure effective fault detection.

2. Materials and Methods

The experimental campaign was conducted using the AV Test Bench produced by AMC Vibro, a platform specialized in the diagnostics of rotating machines. The system, as shown in Figure 1, and schematized in Figure 2, consists of an electric motor, operated under closed-loop speed control, coupled to a gearbox that drives a primary shaft supported by the rolling bearing under study. To replicate industrial operating conditions, a second electric motor, acting as a brake, is connected to the opposite end of the shaft and used as a magnetic brake, applying a controllable torque to the shaft. In this configuration, the primary motor determines the shaft speed, while the secondary motor (brake) independently regulates the torque applied to the shaft.

 doi:10.20944/preprints202604.0395.v1

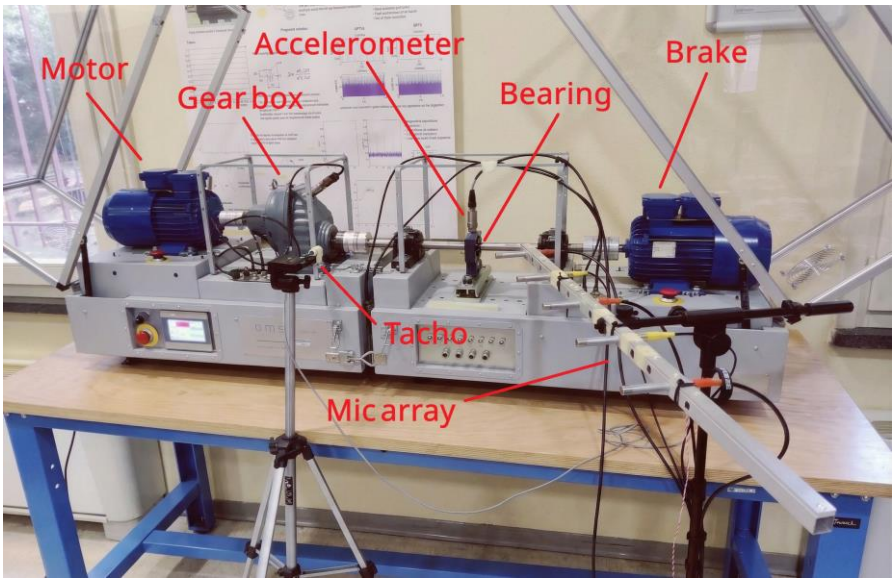

Figure 1. Picture of the experimental test bench for bearing diagnostics, showing the main mechanical components and the integrated sensor array.

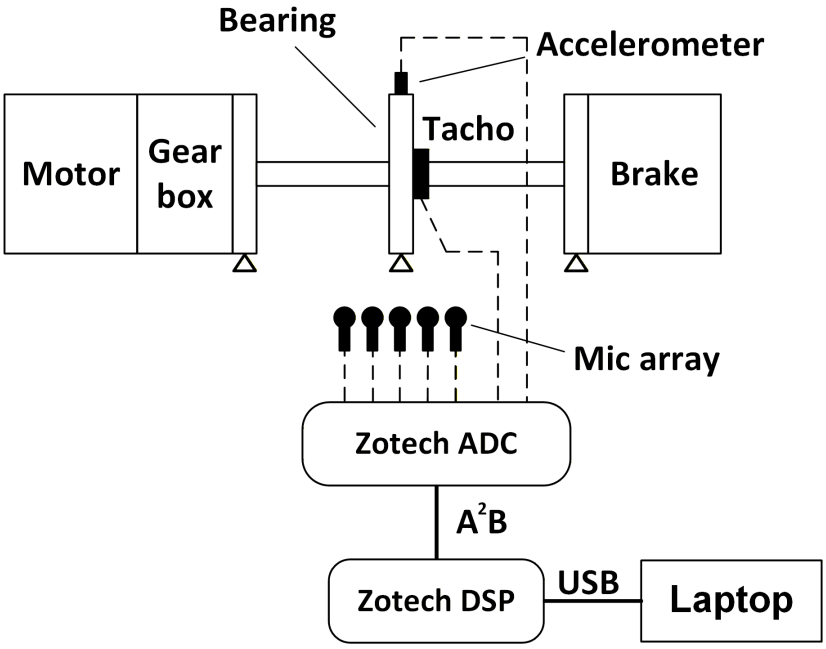

Figure 2. Scheme of the test bench for bearing, including the sensors and the digital acquisition system.

2.1. Sensors and Data Acquisition Devices

The diagnostic system integrates both vibration and acoustic transducers to enable direct performance comparison. In addition, shaft rotation speed is monitored in real time using an RS PRO Diffuse Reflection Photoelectric Sensor optical tachometer. For the vibration measurements, a Monitran MTN/2200M6 industrial IEPE monoaxial accelerometer (Table 1) was securely attached to the bearing housing using a threaded coupling. This sensor serves as a contact-based reference for evaluating the severity of localized bearing defects.

 doi:10.20944/preprints202604.0395.v1

Table 1. Accelerometer Monitran MTN/2200M6, technical data.

Specification	Value
Sensitivity (±10%)	100 mV/g
Measurement Range	±80g
Frequency Range	2 Hz to 10 kHz

For the acoustic monitoring, a linear microphone array consisting of five Brüel & Kjær type 4188 omnidirectional microphones (Table 2) was used for remote detection. The sensors were mounted on a rigid support to eliminate parasitic vibrations and were spaced evenly at 15 cm intervals.

Table 2. Microphone and Preamplifier Bruel&Kjaer 4188-2176, technical data.

Specification	Value
Sensitivity	31.6 mV/Pa
Dynamic Range	19 to 138 dB
Frequency Range	8 Hz to 12.5 kHz

The tachometer sensor, the accelerometer, and five microphones that make up the linear array must be sampled simultaneously. This requires an acquisition system capable of ensuring precise synchronization. For this reason, Zotech's DAQ (Digital Acquisition) system was chosen, based on Analog Devices' A2B bus [29], which allows the transmission of up to 32 signals sampled at 48 kHz and 24 bits over a single UTP (unshielded twisted pair) cable.

This DAQ system, initially developed for the automotive sector, can be applied in many other areas. For example, structural health monitoring [30], industrial condition monitoring [31]-[32], vibration measurement systems [8], and predictive maintenance, which often rely on a large number of sensors that must be sampled simultaneously and in real time. DAQ A2B offers an alternative solution for the synchronous acquisition of multiple sensor signals, while reducing overall system costs through inexpensive cables and low-cost dedicated transceivers. Thanks to its features and low implementation costs, A2B is also particularly suitable for applications with microphone arrays [33,34].

Another benefit of the proposed architecture is the synchronization of the Zotech ADC devices. In fact, the digital bus allows all network nodes to remain synchronized, with minimal latency and very low jitter levels [35]. In the case of a more complex installation with a certain distance between the tachometer, the accelerometer, and the microphone array, the system still guarantees perfect synchronization between the sampled signals.

2.2. Test Conditions

To evaluate the diagnostic effectiveness of the acoustic array in identifying bearing degradation, a comprehensive series of experimental measurements was conducted under various operating conditions for both healthy and defective bearings. The test bearing selected for this study is the SKF YAR 204 2F rolling bearing, whose technical specifications are summarized in Table 3. This model is housed within an SKF TU 504 M cast iron unit, which serves as the primary interface for transmitting radial loads to the bearing. The integration of the YAR 204 2F bearing and the TU 504 M housing is a fundamental design feature of the experimental test rig.

Table 3. SKF YAR 204 2F bearing specifications.

Specification	Value
Number of balls	8
Diameter of balls	7.938 mm
Pitch diameter	33.5 mm
Contact angle	0°

 doi:10.20944/preprints202604.0395.v1

The defect was located on the outer race of the bearing (the size of the damage is about 5 x 3 mm). To simulate this damage, the outer ring was subjected to a controlled thermal etching using an industrial welding machine to induce localized surface damage (Figure 3).

Figure 3. Detailed view of the damaged bearing: (left) assembled SKF YAR 204 2F unit; (right) disassembled outer race highlighting the localized defect (approx. 5 x 3 mm); (center) magnified detail of the spalling area.

The experimental campaign involved testing both healthy and faulty bearings across a range of operating conditions. The choice of speed was determined by the technical specifications of the test rig, which feature a maximum motor speed of 3000 rpm. Accordingly, three equally spaced motor speeds were selected (1000, 2000, and 3000 rpm); given the gear ratio of approximately 2.91:1, these correspond to bearing shaft speeds of approximately 344, 687, and 1031 rpm, respectively. For each speed, three levels of torsional load (0%, 25%, and 50%) were evaluated, equivalent to 0, 2, and 4 Nm. In addition, a constant radial load was applied manually via a load screw acting on the bearing housing. For each condition and sensor, a total of at least 20 s of signal at a sample frequency of 48 kHz was acquired. This allows us to evaluate how operating variables affect the defect's acoustic signature. Moreover, to systematically evaluate the influence of sensor proximity and orientation, the experimental matrix was repeated using three discrete microphone array configurations, as illustrated in Figure 4: center, right, and left positions. In each configuration, the first sensor of the linear array was positioned at a minimum distance of 15 cm from the bearing housing.

Using a proper support with a constant distance of 15 cm between sensors, five distinct measurement points were evaluated simultaneously at distances of 15 cm, 30 cm, 45 cm, 60 cm, and 75 cm. This extended range was chosen to quantify the decrease in fault detection sensitivity as the acoustic signal propagates through the environment.

The experimental setup includes two electric motors: one driving the shaft and one acting as a brake. Both components are potential sources of acoustic emissions that may influence the measurements acquired by microphones. However, no distinct tonal or deterministic disturbances directly attributable to the motors were identified in the recorded signals. Instead, their contribution is considered part of the broadband background noise of the test environment.

This aspect is consistent with the observed limitations of broadband scalar indicators (e.g., RMS and kurtosis), which are significantly affected by environmental and mechanical noise. To mitigate these effects, the analysis focuses on the High-Frequency Resonance Technique (HFRT), which isolates high-frequency resonance bands where fault-related impulsive components dominate and the influence of low-frequency disturbances, such as those generated by motors, is significantly reduced.

 doi:10.20944/preprints202604.0395.v1

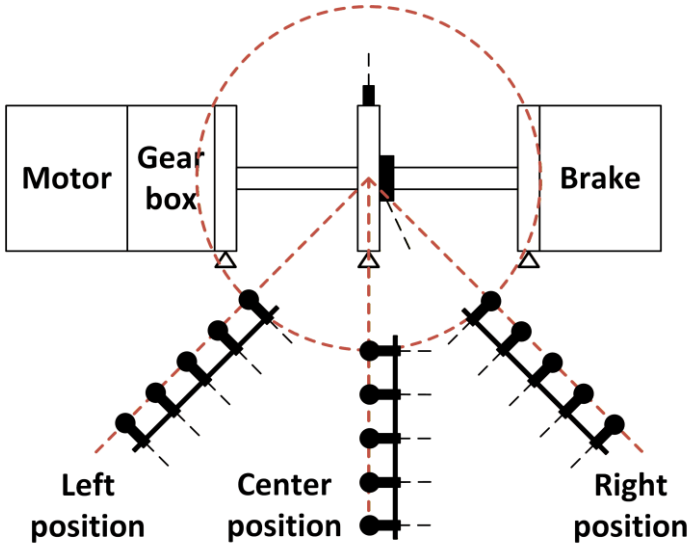

Figure 4. Scheme of microphone array placement diagram. Left and right positions are displaced by 45° with respect to the center position.

2.3. Data Processing and Analysis

Prior to the experimental campaign, all acoustic sensors were calibrated using a Brüel & Kjær Type 4231 sound level calibrator. Calibration was performed at a reference sound pressure level of 94 dB (1 Pa) at 1 kHz, ensuring that voltage outputs were accurately converted to physical pressure units. This procedure was essential to maintain consistency across the array's microphones and to enable reliable calculation of energy-based diagnostic indicators.

The signal processing, including calibration and data preparation, was implemented using Python programming language. At first, all signals were aligned to the first useful pulse of the tachometer and cut to obtain signals of length 20 s. Subsequently, to isolate the relevant frequency content, the accelerometer and microphone signals were processed through fourth-order Butterworth bandpass filters. The accelerometer bandwidth was filtered between 2 Hz and 10 kHz, while the microphone signals were filtered between 8 Hz and 12.5 kHz. To maintain time alignment and phase integrity across both sensor types, a zero-phase filtering technique was employed. These procedures ensured that both vibration and acoustic data were limited to their respective effective operating bandwidths.

After the pre-processing phase, the analysis focused on extracting global features in the time domain, in particular the RMS, CF, and Kurtosis. These broadband indicators were selected to evaluate the diagnostic effectiveness, as the position and distance of the microphones vary, of the computationally efficient features that characterize the entire operating spectrum of both the accelerometer and the microphones.

The investigation began by calculating the RMS and CF values for each sensor configuration and operating condition detailed in Section 2.2. These indicators, which serve respectively as measures of the overall energy content and the signal impulsivity, were defined as follows:

$$RMS = \sqrt{\frac{1}{N}\sum_{i=1}^{N}|x_i|^2}, \quad (1)$$

$$CF = \frac{\max|x_i|}{\sqrt{\frac{1}{N}\sum_{i=1}^{N}|x_i|^2}}, \quad (2)$$

where N is the total number of samples.

The preliminary analysis of global energy indicators, shown in Figure 5, highlights the fundamental challenges of non-contact acoustic monitoring. Figure 5a confirms the reliability of structure-borne vibration as a benchmark: the accelerometer, being directly coupled to the bearing

 doi:10.20944/preprints202604.0395.v1

housing, captures the impulsive energy of the fault with minimal attenuation. The resulting faulty-to-healthy RMS ratio is consistently high, as the sensor is immune to airborne background noise.

In contrast, Figures 5b, 5c, and 5d reveal a poor SNR of the acoustic RMS values captured by the microphone array at various distances for different speed, load, and position configurations. These plots were selected as representative examples of the overall trends observed under all testing conditions. Unlike the vibration-based results, the acoustic scalar indicators show highly inconsistent and unpredictable trends. The energy increase induced by the fault is often obscured by broadband background noise and environmental interference. In several configurations, such as the central position shown in Figure 5c, the RMS values for the healthy bearing are comparable to or even higher than those for the faulty state. Furthermore, the expected decay of energy with increasing distance is often non-linear, likely due to local fluid-dynamic turbulence and acoustic reflections within the test-bench environment.

The analysis was carried out by calculating the CF. Although it is a standard parameter for identifying impulse transients, it has yielded unsatisfactory results in the acoustic domain, failing to clearly distinguish between normal operating conditions and fault conditions. In most configurations, CF values remained statistically indistinguishable, as the impulse peaks from bearing impacts were "masked" by high-energy stationary background noise, which significantly inflated the RMS denominator of the ratio. In conclusion, both the RMS and the CF have proven to be unreliable diagnostic indices.

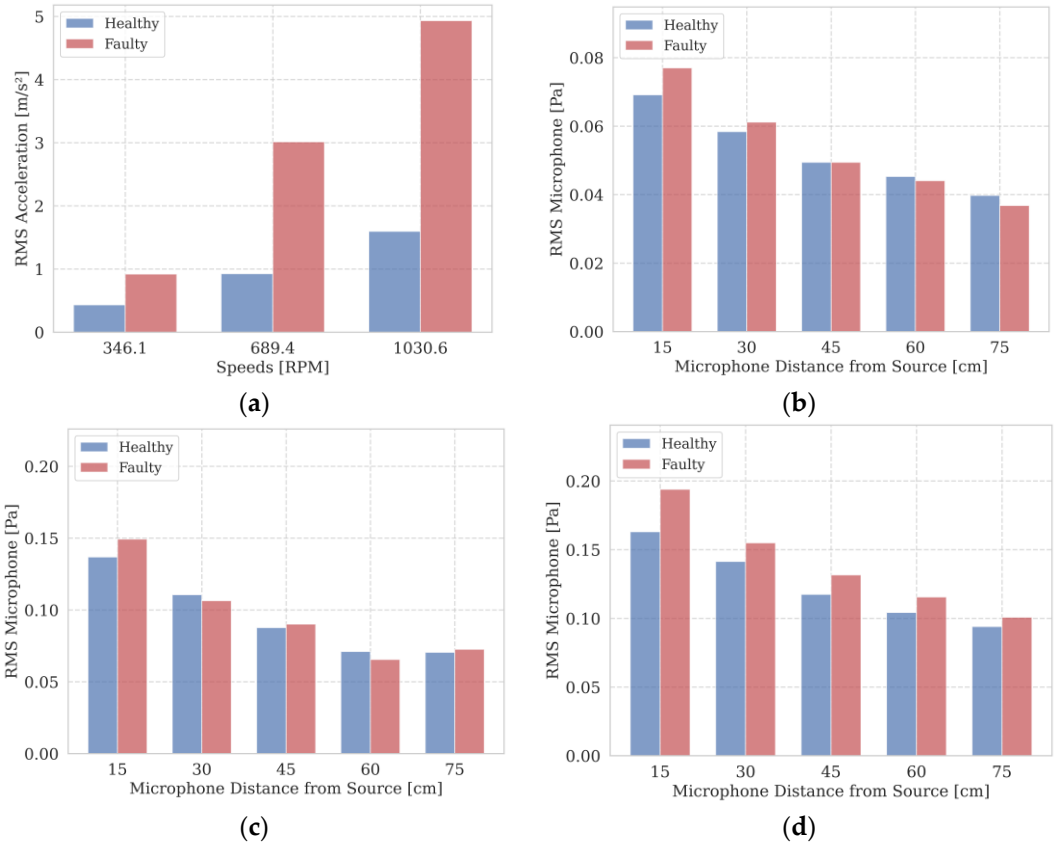

Figure 5. RMS energy levels for healthy vs. faulty bearing: (**a**) Contact-based accelerometer performance at 25% torsional load; (**b**) Acoustic RMS value at 344 rpm (Right position, 25% load); (**c**) Acoustic RMS value at 687 rpm (Central position, 0% load); (**d**) Acoustic RMS value at 1031 rpm (Left position, 25% load).

In addition to energy-based metrics, the Kurtosis was evaluated to determine its sensitivity to the impulsive nature of bearing faults across different sensing modalities. As a dimensionless statistical parameter, Kurtosis measures the "peakedness" of the signal distribution, making it a primary indicator for detecting the transient shocks associated with localized structural degradation. For a discrete signal x consisting of N samples, it is defined as:

 doi:10.20944/preprints202604.0395.v1

$$K = \frac{\frac{1}{N}\sum_{i=1}^{N}(x_i-\bar{x})^4}{\left[\frac{1}{N}\sum_{i=1}^{N}(x_i-\bar{x})^2\right]^2}, \quad (3)$$

where $\bar{x}$ represents the mean value of the signal.

In Figure 6, specific operating conditions were selected for both the accelerometer and the microphones to illustrate the metric's general trend. As shown in Figure 6a, the contact accelerometer provides highly sensitive fault detection even at lower rotational speeds, with Kurtosis values exceeding 70 for the fault condition compared to the reference value of approximately 3 for the healthy bearing. This high value confirms the presence of strong periodic impulsive shocks generated by the localized defect. However, a significant downward trend in Kurtosis is observed as the rotational speed increases from 344 rpm to 1031 rpm. This phenomenon is attributed to increases in the repetition frequency of fault impacts and in broadband background noise, which together lead to a "blurring" effect in the time domain, making the signal statistically more similar to Gaussian noise and thus reducing the sensitivity of this scalar indicator.

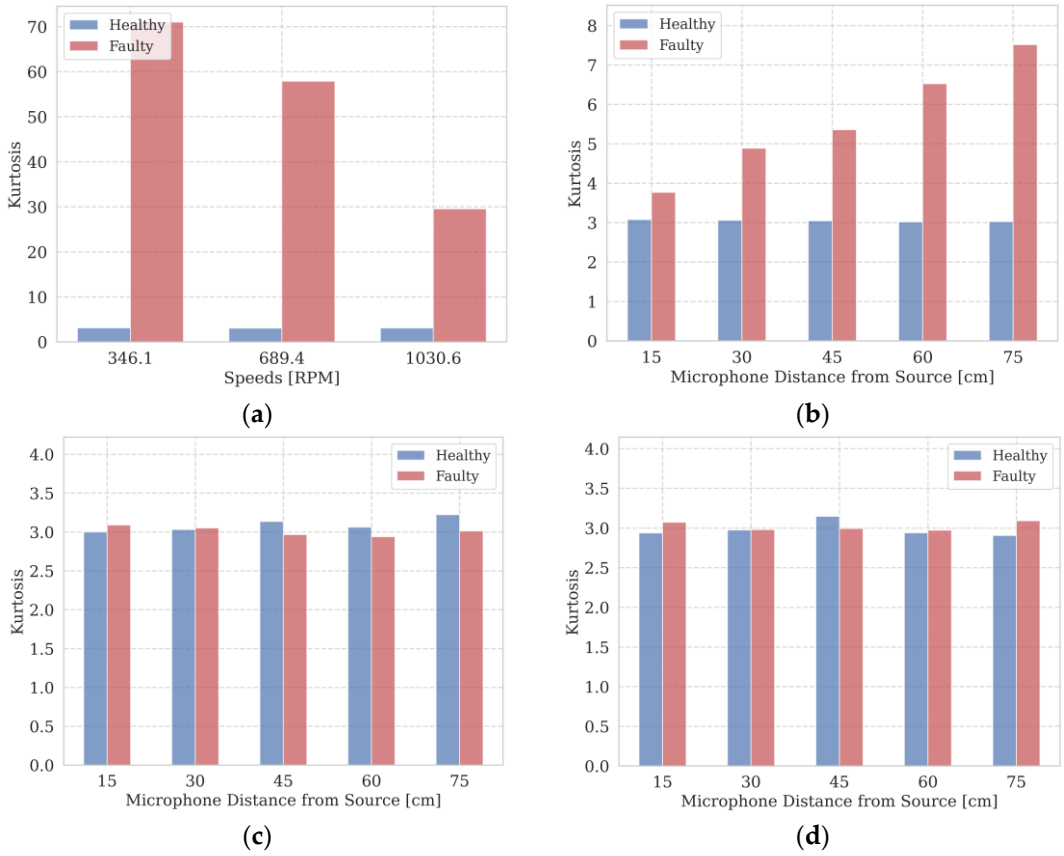

Figure 6. Kurtosis values for healthy vs. faulty signals: (**a**) Contact-based accelerometer performance at 25% torsional load; (**b**) Acoustic Kurtosis at 344 rpm (Central position, 25% load); (**c**) Acoustic Kurtosis at 687 rpm (Right position, 0% load); (**d**) Acoustic Kurtosis at 1031 rpm (Left position, 50% load).

The analysis of acoustic signals, presented in Figures 6b, 6c, and 6d, further highlights the challenges of remote monitoring. For microphones, Kurtosis values remain consistently low, fluctuating near the theoretical value of 3 for a Gaussian distribution, regardless of bearing conditions. In many configurations, such as those shown at higher speeds and with a 25% load (Figure 6d), the Kurtosis fails to distinguish between normal and defective conditions. Although some localized increases are visible at low speeds (Figure 6b), the overall trend is inconsistent across different distances and positions. These results demonstrate that, as with the RMS and CF values, the overall Kurtosis of the acoustic signals is severely compromised by the dominant ambient background noise, which masks the low-energy impulse traces associated with bearing failure.

 doi:10.20944/preprints202604.0395.v1

The spatial correlation observed in Figure 7 provides a quantitative measure of the signal's integrity as it propagates through the industrial environment. The maximum cross-correlation coefficient effectively represents the ratio between the coherent energy (the fault transients) and the total pressure field energy captured by the sensors. The steep decay from 1.0 to approximately 0.3 suggests that by the time the wavefront reaches 75 cm, the signal is dominated by uncorrelated components, such as ambient background noise and multi-path reflections. Another observation is the load-independence of the decay curves: the overlap between 0%, 25%, and 50% load conditions confirms that the loss of coherence is an inherent property of the acoustic transmission path and the test-bench acoustics, rather than a function of fault severity. Mathematically, a correlation of 0.3 indicates that the SNR has dropped to a level where the deterministic component of the bearing impact is almost entirely "smeared" into the stochastic background. This lack of statistical differentiation reinforces the need to move beyond broadband metrics in the time domain toward a frequency-selective envelope analysis to extract reliable diagnostic information from non-contact sensors.

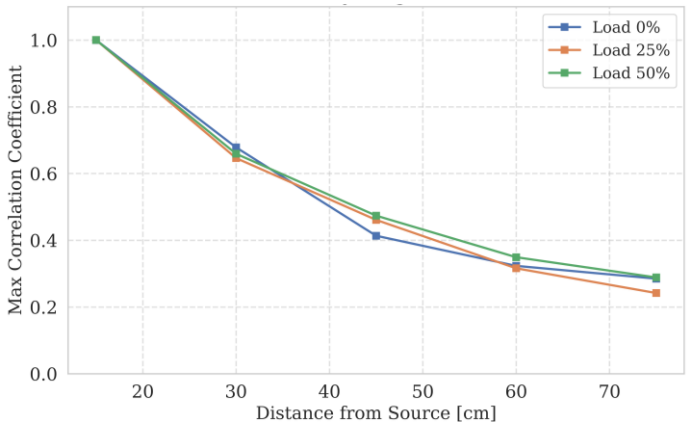

Figure 7. Spatial decay of the maximum cross-correlation coefficient as a function of distance from the acoustic source. The analysis refers to the Right Position configuration at a rotational speed of 687 rpm under different torsional load conditions.

For this reason, the analysis focused on the HFRT [20]. The proposed methodology uses a bandpass filter to isolate high-frequency structural resonances excited by impulsive impacts between rotating elements and the localized defect. By focusing on these specific spectral regions, the technique effectively suppresses the dominant low-frequency interference that characterizes the operating environment. This step is particularly critical for acoustic monitoring, as microphones are inherently sensitive to mechanical and aerodynamic noise. The resulting signal is then demodulated to extract the low frequencies characteristic of the damage, identified using kinematic equations based on the geometry of the bearing:

$$BPFO = \frac{n}{2} f_r \left(1 - \frac{BD}{PD} cos\beta\right), \quad (4)$$

$$BPFI = \frac{n}{2} f_r \left(1 + \frac{BD}{PD} cos\beta\right), \quad (5)$$

$$BFF = \frac{PD}{BD} f_r \left[1 - \left(\frac{BD}{PD} cos\beta\right)^2\right], \quad (6)$$

$$FTF = \frac{1}{2} f_r \left(1 - \frac{BD}{PD} cos\beta\right), \quad (7)$$

where f_r denotes the shaft rotational frequency in Hz, n represents the number of rolling elements, BD and PD are the ball diameter and the pitch circle diameter, respectively, and β is the contact angle. The theoretical fault frequencies include the Ball Pass Frequency Outer race (BPFO), the Ball

 doi:10.20944/preprints202604.0395.v1

Pass Frequency Inner race (BPFI), the Ball Fault Frequency (BFF), and the Fundamental Train Frequency (FTF). This study will focus on the defect induced, as described in Sect. 2.2, on the outer ring bearing (BPFO). The characteristic frequencies calculated for each of the rotational speeds under analysis are summarized in Table 4.

Table 4. Characteristic fault frequencies for each rotational speed under analysis.

Speed [rpm]	BPFO	BPFI	BFF	FTF
344	17.56 Hz	28.46 Hz	22.92 Hz	2.19 Hz
687	35.03 Hz	56.79 Hz	45.72 Hz	4.38 Hz
1031	52.40 Hz	84.94 Hz	68.38 Hz	6.55 Hz

To identify the optimal filter band for fault detection, the Spectral Kurtosis (SK) was calculated for each acoustic signal [36,37]. Unlike traditional broadband indicators, SK provides a frequency-resolved measure of impulsivity, enabling the localization of non-stationary transients within specific resonance bands. As illustrated in the representative example in Figure 8, the SK analysis reveals a significant concentration of impulsive energy in the high-frequency range.

Specifically, the microphones positioned at 15 cm and 30 cm exhibit prominent kurtosis peaks between 8 kHz and 12 kHz, coinciding with structural resonances excited by bearing impacts. It can be observed that, while the peak amplitude decreases with increasing distance due to a reduction in SNR, the frequency localization of the maximum impulsivity remains remarkably stable. This indicates that the acoustic signature is dominated by the transfer function of the mechanical structure rather than the characteristics of the acoustic path. Based on these findings, the 8–12 kHz range was identified as the optimal band for filtering. This approach effectively isolates the spectral region of maximum structural resonance, thereby optimizing the SNR for the subsequent envelope analysis (HFRT).

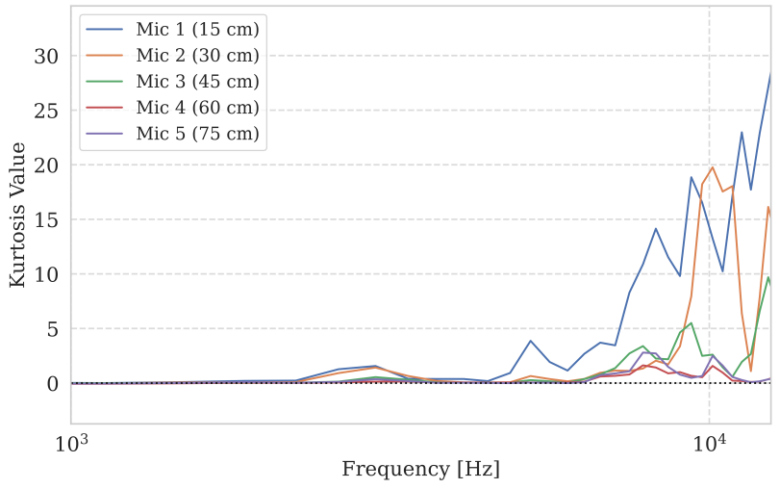

Figure 8. Distribution of 1/3 octave band Kurtosis for the microphones in the Right position (687 rpm, 0% load) under faulty conditions.

To extract the diagnostic information, the raw signals were band-pass filtered in this specific range and subsequently demodulated by calculating the modulus of the analytical signal via the Hilbert Transform. The resulting envelope Power Spectral Density (PSD) is presented in Figure 9, which compares the diagnostic performance of the reference accelerometer (9a) and the microphone at 15 cm (9b) under a 687 rpm speed and 25% torsional load. In both measures, the BPFO harmonics (green dashed lines) emerge with high spectral clarity against the healthy baseline (blue line), providing an unmistakable signature of the outer raceway defect. In the raw acoustic signal, the 3rd rotational harmonic (≈ 34.3 Hz) and the fundamental BPFO (≈ 35.8 Hz) are spectrally adjacent, a

 doi:10.20944/preprints202604.0395.v1

condition that typically leads to spectral masking in broadband Fourier analysis. However, the HFRT effectively bypasses this issue. Since the shaft's rotational motion is a low-frequency phenomenon that does not excite high-frequency structural resonances, its contribution is naturally suppressed during the band-pass filtering stage. Consequently, the rotational harmonics (orange dashed lines) appear significantly attenuated, with the energy almost exclusively concentrated at the fault frequencies. For the acoustic sensor (Figure 9b), this means that, despite airborne transmission, the SNR in the envelope domain is sufficiently high to produce a "clean" harmonic series. This demonstrates that, although the acoustic signal is overall noisier (as shown by the scalar indicator analysis), its stochastic-impulsive content is preserved and can be successfully recovered through frequency-selective demodulation.

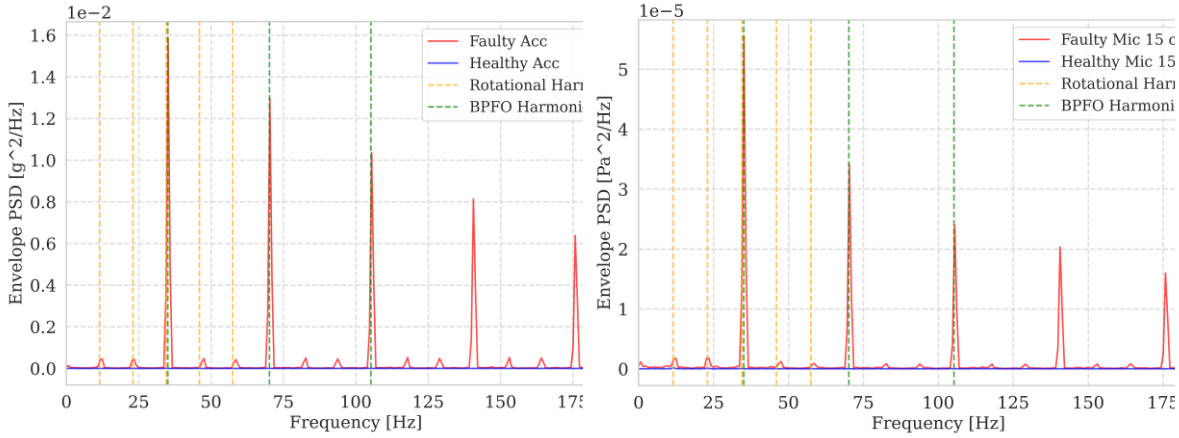

(**a**) (**b**)

Figure 9. Envelope PSD for (a) the accelerometer and (b) the microphone (15 cm distance) at 687 rpm and 25% load. The spectra compare the healthy baseline (blue line) with the faulty condition (red line). Vertical dashed lines indicate the theoretical BPFO harmonics (green) and shaft rotational harmonics (orange).

3. Results

This section provides a detailed analysis of the experimental results obtained from monitoring the acoustics emission of rolling bearings. This analysis is performed considering different loads, distances, and sensor positions. The results are presented in two stages to highlight the transition from overall energy assessment to targeted fault identification. First, the performance of traditional broadband scalar indicators, namely RMS and kurtosis, is evaluated. Next, the results of the HFRT are discussed, with particular attention to the influence of sensor position on its ability to isolate impulsive signatures related to faults from dominant environmental and aerodynamic background noise..

3.1. Performance of Broadband Scalar Indicators (RMS and Kurtosis)

To ensure a consistent comparative metric between the broadband scalar indicators and the subsequent HFRT, the results are presented as a dimensionless ratio of the faulty to healthy conditions. This normalization approach was specifically adopted to allow for a direct performance comparison across different sensing modalities and diagnostic metrics.

The diagnostic performance of the acoustic energy indicator at a 50% torsional load is summarized in Figure 10, which presents the RMS ratio (faulty/healthy) for the three microphone array placements: Central (a), Right (b), and Left (c). Regardless of the spatial configuration or the distance from the source, the calculated ratios exhibit no significant trend, oscillating within a narrow range between 0.8 and 1.3. Considering that a ratio of 1.0 represents the theoretical threshold for fault detection, these values indicate that when the fault-induced energy is significantly lower than the ambient noise variance, the resulting ratio becomes dominated by stochastic fluctuations rather than

 doi:10.20944/preprints202604.0395.v1

the health state of the bearing. These results demonstrate that distance and sensor positioning cannot compensate for the lack of frequency selectivity, reinforcing the conclusion that broadband acoustic power is a fundamentally unreliable feature for remote bearing diagnostics.

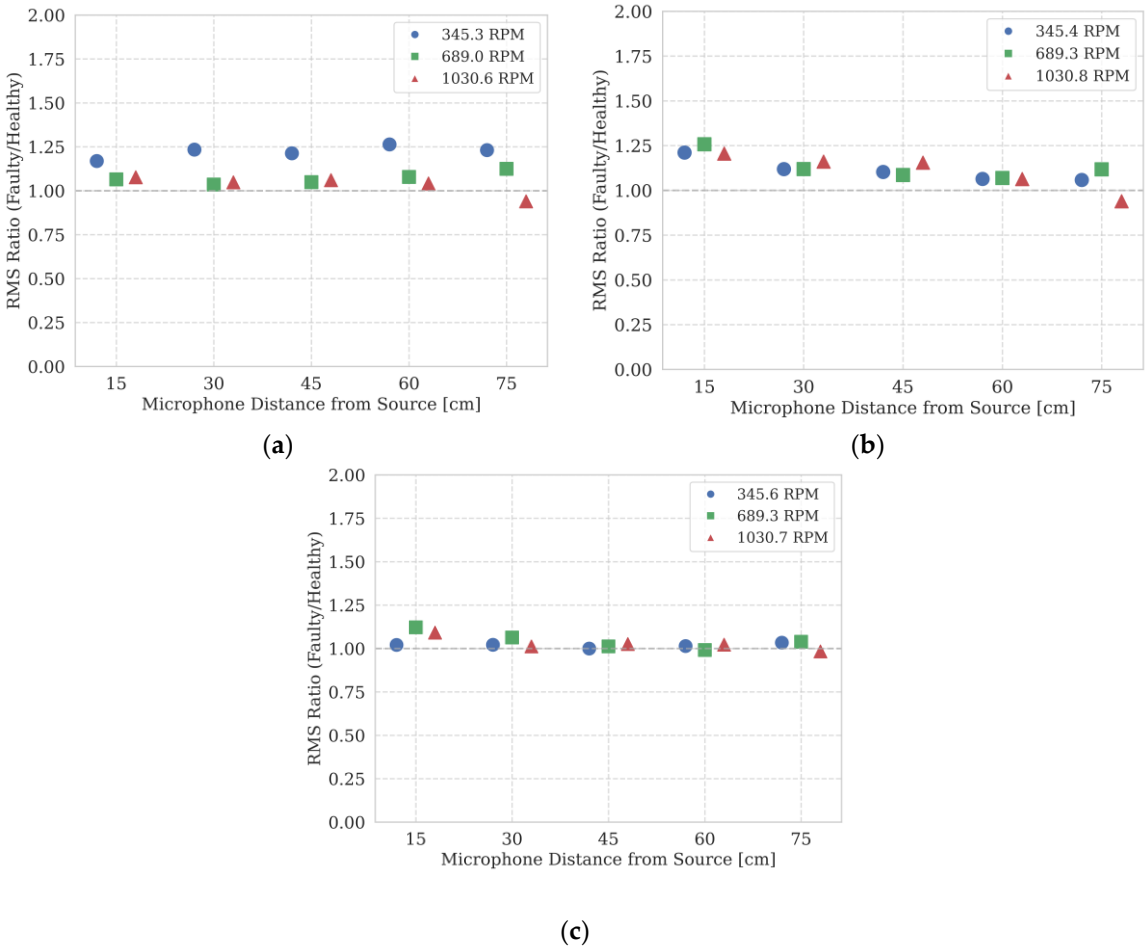

Figure 10. Acoustic RMS ratio (faulty/healthy) at 50% torsional load for (a) Central, (b) Right, and (c) Left microphone array placements. The ratio is plotted as a function of source distance (15–75 cm) for three rotational speeds: 344 rpm (blue circles), 687 rpm (green squares), and 1031 rpm (red triangles). The horizontal dashed line at 1.0 represents the detection threshold.

Similar to the RMS results, the global kurtosis values calculated for the acoustic signals, previously illustrated in Figure 6, confirm the limitations of scalar time-domain indicators. While the contact accelerometer captures the impulsive nature of the bearing defect, yielding kurtosis values significantly above the gaussian threshold of 3, the microphones exhibit a flat behavior across all distances and rotational speeds. As shown in Figures 6 (b–d), the acoustic kurtosis consistently hovers around 3, indicating that the discrete shocks generated by the defect are statistically indistinguishable from background noise. This lack of statistical differentiation, even at a distance of 15 cm, provides further empirical evidence that broadband scalar metrics are inadequate for reliable non-contact bearing diagnostics in industrial-like environments, thereby necessitating the adoption of more sophisticated frequency-selective techniques.

3.2. HFRT and Envelope Spectral Analysis

Unlike broadband scalar indicators, the application of HFRT successfully reveals the impulsive nature of the bearing defect, which would otherwise be masked by background noise. Figure 11 illustrates the envelope PSD ratio (faulty/healthy) obtained under 50% torsional loading conditions. In this view, only data from the closest microphone (15 cm) are presented to maintain graphical

 doi:10.20944/preprints202604.0395.v1

clarity, enabling a focused assessment of how the sensor's spatial orientation affects diagnostic sensitivity. The results demonstrate that HFRT effectively isolates the BPFO's fundamental frequency and its higher-order harmonics, with exceptional spectral clarity across a range of rotational speeds. Notably, the magnitude of these ratios is several orders of magnitude higher than that obtained with broadband metrics; while RMS ratios struggled to exceed 1.3, HFRT ratios reached values up to 40 dB, confirming the absolute superiority of frequency-selective demodulation for remote acoustic monitoring.

The spatial analysis reveals a systematic directional bias. The Right position consistently outperforms the others, particularly at 687 and 1031 rpm. It is important to emphasize that this superior performance is not merely a result of higher absolute acoustic levels, but specifically of a higher SNR of the fault-induced transients. While the motor brake coupling may contribute to higher overall acoustic emissions on the right side of the test rig, its primary impact is likely the modulation of the bearing's internal load zone orientation. This hypothesis is supported by comparing results across different loading conditions: under no-load operation, the extreme spatial bias toward the right position is significantly reduced, with the right and left sensors exhibiting more comparable diagnostic ratios. However, this asymmetry intensifies with the introduction of torsional load (25% and 50%), confirming that mechanical stress preferentially amplifies the defect's acoustic signature in that quadrant. In contrast, the center position consistently exhibits the lowest performance across all test cases. This persistent attenuation can be attributed to the bearing housing, which acts as a physical acoustic shield, creating a shadowing effect that obstructs the direct propagation path between the source and the microphones. The signal reaching these sensors is primarily composed of diffracted waves and reflections, which have inherently lower energy than the direct-path waves captured by the side positions, thereby severely limiting the SNR, even after advanced processing via HFRT.

Furthermore, rotational speed was found to have a marked influence on diagnostic sensitivity. At higher rotation speeds, the increased impact energy further elevates the envelope ratios, enhancing fault detectability even at greater distances. These findings suggest that effective remote acoustic monitoring is not solely distance-dependent; rather, it is critically linked to signal transmission paths and physical obstructions within the machinery.

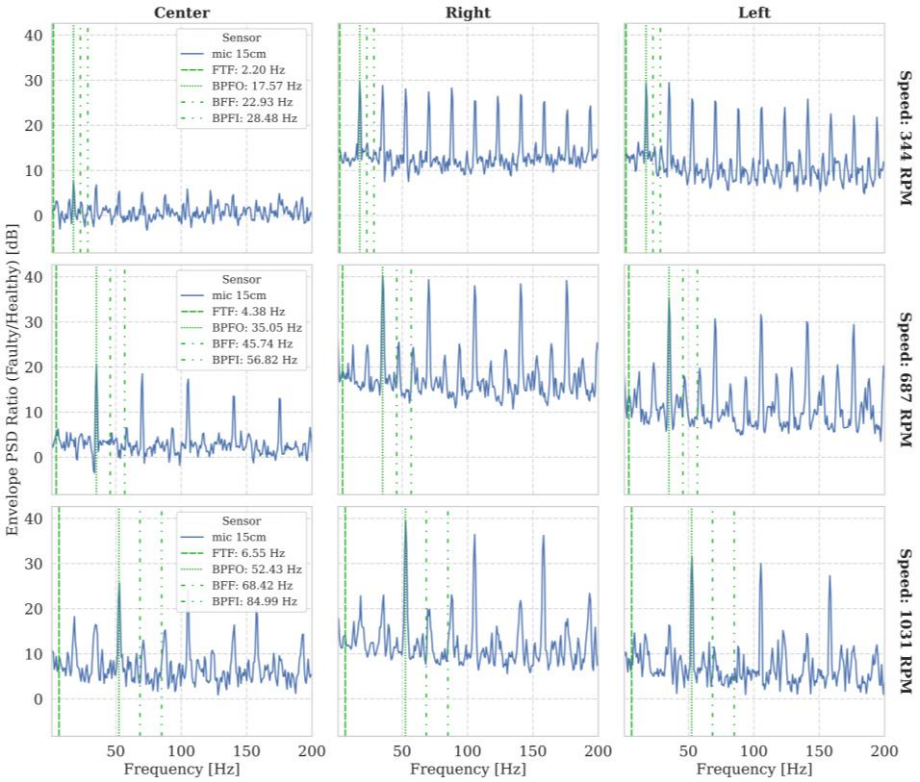

 doi:10.20944/preprints202604.0395.v1

Figure 11. Matrix of acoustic Envelope PSD Ratio (faulty/healthy) in dB obtained under 50% torsional load. The analysis focuses on the closest sensor (15 cm distance) to highlight the maximum diagnostic sensitivity across the three array positions (columns) and rotational speeds (rows). Green vertical lines represent the theoretical characteristic frequencies for the tested bearing (FTF, BPFO, BFF, BPFI), updated for each speed row.

The diagnostic performance across the tested range reveals a critical trade-off between absolute signal intensity and localized interference. Although the 15 cm position is unequivocally the most effective for capturing high-energy signal components, it is uniquely susceptible to proximity effects. As illustrated in the broadband PSD (Figure 12), the closest microphone captures a prominent low-frequency "hump" (below 100 Hz) caused by aerodynamic turbulence from the bearing's rotation. While such near-field disturbances often compromise traditional scalar indicators, frequency-selective techniques, like HFRT, effectively bypass this noise by isolating high-frequency resonant bands.

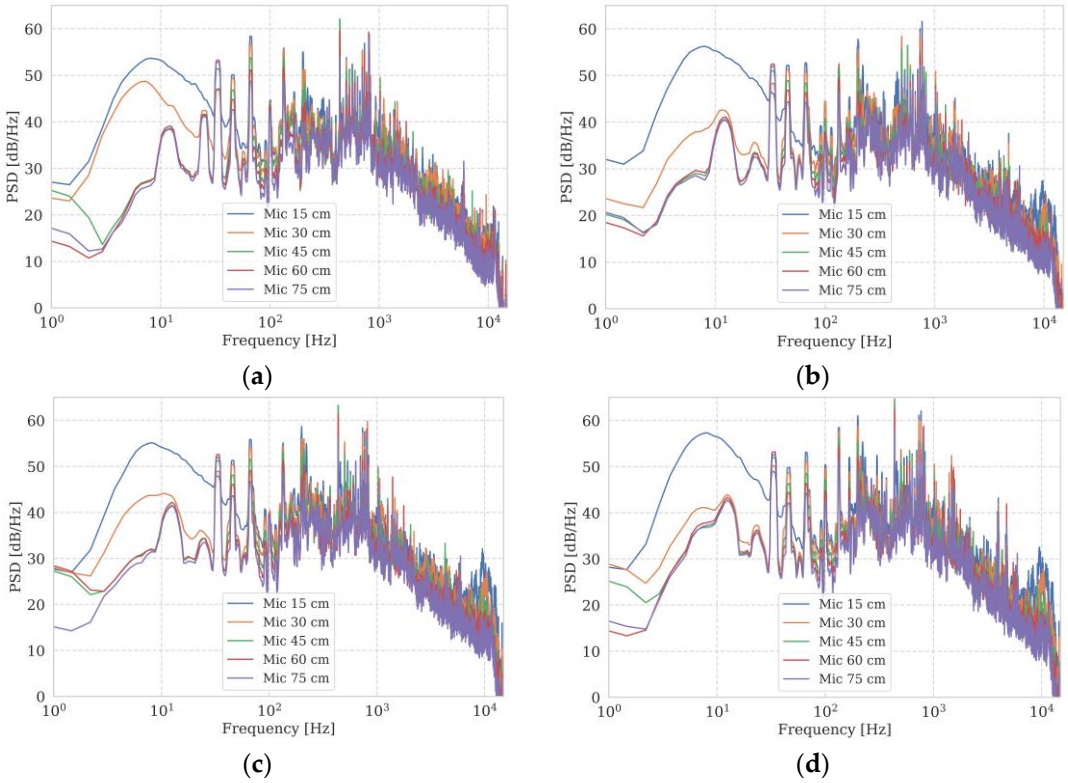

Figure 12. Multi-panel comparison of the broadband acoustic PSD captured at 687 rpm in the Right array position. The panels illustrate four distinct operational states: (a) Healthy baseline at 25% torsional load; (b) Faulty condition at 0% load; (c) Faulty condition at 25% load; and (d) Faulty condition at 50% load. Colored lines represent the five microphone distances, from 15 cm (blue) to 75 cm (purple).

The spatial decay of the fault-related spectral energy is analyzed in Figure 13a, which tracks the cumulative energy of the first three BPFO harmonics across the microphone array. The graph shows consistent attenuation across all tested speeds; in particular, the cumulative peak amplitude declines sharply as the distance between the sensor and the source increases. From the reference position at 15 cm to the distal microphone at 75 cm, diagnostic energy levels are reduced by more than 50 dB, confirming the impact of distance-related signal degradation on non-contact acoustic detection. It is important to note that this decrease represents a deterioration in the SNR rather than a simple reduction in sound pressure level. Interestingly, the decay curves exhibit a slight plateauing effect between 60 cm and 75 cm. This suggests that at greater distances, the signal reaches a 'reverberant floor' within the test-bench enclosure, where multi-path reflections begin to compensate for the direct-path attenuation.

 doi:10.20944/preprints202604.0395.v1

Finally, Figure 13b underscores the robustness of the proposed method by examining the most challenging experimental configuration: the minimum operating speed (344 rpm) at the maximum sensor distance (75 cm). Despite a 50 dB drop in cumulative energy, the HFRT-processed spectrum yields a prominent BPFO peak with a 14 dB margin above the noise floor. This demonstrates that while distance-related energy loss is inevitable, the diagnostic information remains reliably recoverable. Consequently, remote acoustic monitoring has emerged as a feasible and reliable solution for industrial environments where close-range sensor installation is limited.

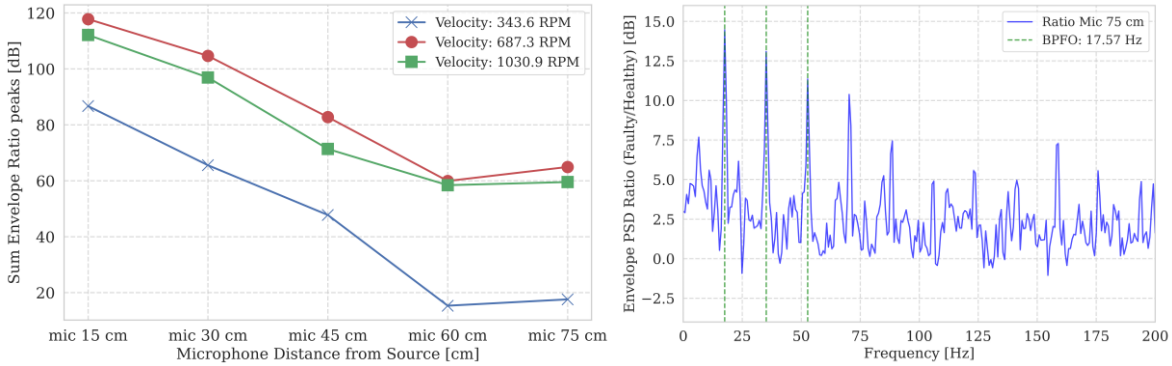

(**a**) (**b**)

Figure 13. Diagnostic performance of the HFRT technique at 50% load: (a) Trend of the cumulative energy of the first three diagnostic harmonics ($BPFO_{1-3}$) in dB as a function of microphone distance; (b) Detail of the envelope spectrum ratio in dB for the 344 rpm case at 75 cm. Dashed vertical lines indicate the theoretical BPFO fault frequency and harmonics.

4. Discussion

The experimental results demonstrate that microphone distance and spatial orientation are critical parameters that significantly influence the detectability of acoustic faults in rotating machinery. This work shows that, for measurement microphones with limited bandwidth, traditional diagnostic parameters such as RMS, CF and kurtosis are insufficient for fault identification, regardless of sensor distance or spatial orientation. Consequently, the implementation of a more advanced analysis technique—the HFRT—became necessary to successfully isolate and clearly identify bearing damage.

The failure of broadband indicators is primarily driven by the overwhelming presence of low-frequency mechanical and aerodynamic noise, which masks the defect's impulsive energy in the time domain. Specifically, the 15 cm position was uniquely affected by a prominent low-frequency "hump" below 100 Hz. This phenomenon, attributed to near-field aerodynamic turbulence generated by the bearing's rotation, proved to be load-invariant, as it appeared consistently in both healthy and faulty spectra regardless of the radial load. By isolating high-frequency resonant bands, HFRT effectively bypasses these localized disturbances, thereby maintaining a high SNR across all tested speeds.

Spatial orientation provided further critical insights into the acoustic transmission paths. The central position consistently exhibited the poorest performance because the bearing housing acts as a physical barrier, creating a shadowing effect that attenuates the high-frequency resonant components necessary for envelope analysis. Conversely, the right position showed exceptional sensitivity under load, with diagnostic ratios exceeding 40 dB. This suggests that the torque induced by the motor brake assembly modulates the bearing's internal load zone, preferentially amplifying acoustic emissions toward that specific quadrant. This hypothesis is validated by the disappearance of such spatial bias under no-load (0%) conditions, where the right and left positions exhibited more symmetrical performance. Ultimately, this study proves that standard measurement microphones with a limited bandwidth (up to 12.5 kHz) remain highly viable for reliable remote diagnostics up to 75 cm, provided that spatial obstructions are avoided and advanced demodulation is employed.

 doi:10.20944/preprints202604.0395.v1

Future research should explore several promising avenues to further enhance the field of remote acoustic diagnostics. Investigating the influence of distance using ultrasonic sensors could reveal whether operating at frequencies beyond 20 kHz further improves the SNR by distancing the diagnostic band from common industrial noise floors. Additionally, characterizing the impact of multi-source background noise in authentic industrial settings is necessary to evaluate the robustness of the HFRT against cross-talk from adjacent machinery. The implementation of microphone arrays for beamforming represents another critical step, as spatial filtering could isolate bearing emissions at even greater distances and in complex environments with significant reflections. Finally, the development of machine learning algorithms for the automated selection of optimal resonance bands would reduce the reliance on manual expert tuning, thereby facilitating the transition toward autonomous, real-time industrial monitoring systems.

Author Contributions: "Conceptualization, E.V., A.T. and E.M.; methodology, E.V., A.T. and E.M.; software, E.V., A.T and L.F.; validation, E.M.; formal analysis, E.V. and A.T.; investigation, E.V. and E.M.; resources, A.T. and E.M.; data curation, E.A. and L.F.; writing—original draft preparation, E.V., A.T. and E.M.; writing—review and editing, E.V., A.T., E.A., M.C., L.F. and E.M.; visualization, E.V., M.C. and E.M.; supervision, A.T. and E.M.; project administration, E.M. and M.C. All authors have read and agreed to the published version of the manuscript.".

Funding: this research was partially funded by the PR-FESR Emilia-Romagna 2021-2027, Priorità 1 - Azione 1.1.2, D.G.R. n. 2097/2022, Project: "Piattaforma di MANutenzione predittiva per il REtroFItting sostenibile di impianti e macchinari esistenti nel sistema produttivo dell'Emilia-Romagna (REFIMAN)", CUP F67G22000290003.

Conflicts of Interest: The authors declare no conflicts of interest.

Abbreviations

The following abbreviations are used in this manuscript:

RMS	Root Mean Square
HFRT	High Frequency Resonance Technique
SK	Spectral Kurtosis
CF	Crest Factor
SNR	Signal to Noise Ratio
DAQ	Digital Acquisition
UTP	Unshielded Twisted Pair
ADC	Analog to Digital Converter
BPFO	Ball Pass Frequency Outer race
BPFI	Ball Pass Frequency Inner race
BFF	Ball Fault Frequency
FTF	Fundamental Train Frequency
PSD	Power Spectral Density
RPM	Revolution Per Minute

References

1. Kannan, V.; Zhang, T.; Li, H. A Review of the Intelligent Condition Monitoring of Rolling Element Bearings. *Machines* **2024**, *12*, 484, doi:10.3390/machines12070484.
2. Sun, B.; Sheng, Z.; Song, P.; Sun, H.; Wang, F.; Sun, X.; Liu, J. State-of-the-Art Detection and Diagnosis Methods for Rolling Bearing Defects: A Comprehensive Review. *Applied Sciences* **2025**, *15*, 1001, doi:10.3390/app15021001.
3. Wei, Y.; Li, Y.; Xu, M.; Huang, W. A Review of Early Fault Diagnosis Approaches and Their Applications in Rotating Machinery. *Entropy* **2019**, *21*, 409, doi:10.3390/e21040409.

 doi:10.20944/preprints202604.0395.v1

4. Orhan, S.; Aktürk, N.; Çelik, V. Vibration Monitoring for Defect Diagnosis of Rolling Element Bearings as a Predictive Maintenance Tool: Comprehensive Case Studies. *NDT & E International* **2006**, *39*, 293–298, doi:10.1016/j.ndteint.2005.08.008.
5. Wang, J.; Liang, Y.; Zheng, Y.; Gao, R.X.; Zhang, F. An Integrated Fault Diagnosis and Prognosis Approach for Predictive Maintenance of Wind Turbine Bearing with Limited Samples. *Renew. Energy* **2020**, *145*, 642–650, doi:10.1016/j.renene.2019.06.103.
6. Cerrada, M.; Sánchez, R.-V.; Li, C.; Pacheco, F.; Cabrera, D.; Valente de Oliveira, J.; Vásquez, R.E. A Review on Data-Driven Fault Severity Assessment in Rolling Bearings. *Mech. Syst. Signal Process.* **2018**, *99*, 169–196, doi:10.1016/j.ymssp.2017.06.012.
7. Zhang, S.; Zhang, S.; Wang, B.; Habetler, T.G. Deep Learning Algorithms for Bearing Fault Diagnostics—A Comprehensive Review. *IEEE Access* **2020**, *8*, 29857–29881, doi:10.1109/ACCESS.2020.2972859.
8. McFadden, P.D.; Smith, J.D. Model for the Vibration Produced by a Single Point Defect in a Rolling Element Bearing. *J. Sound Vib.* **1984**, *96*, 69–82, doi:10.1016/0022-460X(84)90595-9.
9. Randall, R.B.; Antoni, J. Rolling Element Bearing Diagnostics—A Tutorial. *Mech. Syst. Signal Process.* **2011**, *25*, 485–520, doi:10.1016/j.ymssp.2010.07.017.
10. Romanssini, M.; de Aguirre, P.C.C.; Compassi-Severo, L.; Girardi, A.G. A Review on Vibration Monitoring Techniques for Predictive Maintenance of Rotating Machinery. *Eng* **2023**, *4*, 1797–1817, doi:10.3390/eng4030102.
11. Jardine, A.K.S.; Lin, D.; Banjevic, D. A Review on Machinery Diagnostics and Prognostics Implementing Condition-Based Maintenance. *Mech. Syst. Signal Process.* **2006**, *20*, 1483–1510, doi:10.1016/j.ymssp.2005.09.012.
12. Wang, H.; Xie, J. Fault Diagnosis of Rolling Bearings Based on Acoustic Signals in Strong Noise Environments. *Applied Sciences* **2025**, *15*, 1389, doi:10.3390/app15031389.
13. Li, C.; Chen, C.; Gu, X. Acoustic-Based Rolling Bearing Fault Diagnosis Using a Co-Prime Circular Microphone Array. *Sensors* **2023**, *23*, 3050, doi:10.3390/s23063050.
14. Voltolini, E.; Monaco, M.; Armelloni, E.; Cocconcelli, M.; Toscani, A.; Immovilli, F.; Manconi, E. Analysis of Defects in Rolling Bearings Using Vibroacoustic and Ultrasonic Techniques. In Proceedings of the Proceedings of the 11th Convention of the European Acoustics Association Forum Acusticum / EuroNoise 2025; European Acoustics Association: Málaga, Spain, December 25 **2025**; pp. 2079–2086.
15. Orman, M.; Rzeszucinski, P.; Tkaczyk, A.; Krishnamoorthi, K.; Pinto, C.T.; Sulowicz, M. Bearing Fault Detection with the Use of Acoustic Signals Recorded by a Hand-Held Mobile Phone. In Proceedings of the 2015 International Conference on Condition Assessment Techniques in Electrical Systems (CATCON); IEEE, December **2015**; pp. 252–256.
16. Li, C.; Chen, C.; Gu, X. Acoustic-Based Rolling Bearing Fault Diagnosis Using a Co-Prime Circular Microphone Array. *Sensors* **2023**, *23*, 3050, doi:10.3390/s23063050.
17. Kim, Y.-H.; Tan, A.C.C.; Mathew, J.; Yang, B.-S. Condition Monitoring of Low Speed Bearings: A Comparative Study of the Ultrasound Technique Versus Vibration Measurements. In *Engineering Asset Management*; Springer London: London; pp. 182–191.
18. Park, J.; Kim, S.; Choi, J.-H.; Lee, S.H. Frequency Energy Shift Method for Bearing Fault Prognosis Using Microphone Sensor. *Mech. Syst. Signal Process.* **2021**, *147*, 107068, doi:10.1016/j.ymssp.2020.107068.
19. Verellen, T.; Verbelen, F.; Stockman, K.; Steckel, J. Beamforming Applied to Ultrasound Analysis in Detection of Bearing Defects. *Sensors* **2021**, *21*, 6803, doi:10.3390/s21206803.
20. McFadden, P.D.; Smith, J.D. Vibration Monitoring of Rolling Element Bearings by the High-Frequency Resonance Technique — a Review. *Tribol. Int.* **1984**, *17*, 3–10, doi:10.1016/0301-679X(84)90076-8.
21. Mishra, S.K.; Shakya, P.; Babureddy, V.; Ajay Vignesh, S. An Approach to Improve High-Frequency Resonance Technique for Bearing Fault Diagnosis. *Measurement* **2021**, *178*, 109318, doi:10.1016/j.measurement.2021.109318.
22. Moumene, I.; Ouelaa, N. Application of the Wavelets Multiresolution Analysis and the High-Frequency Resonance Technique for Gears and Bearings Faults Diagnosis. *The International Journal of Advanced Manufacturing Technology* **2016**, *83*, 1315–1339, doi:10.1007/s00170-015-7436-0.

 doi:10.20944/preprints202604.0395.v1

23. Tandon, N.; Choudhury, A. A Review of Vibration and Acoustic Measurement Methods for the Detection of Defects in Rolling Element Bearings. *Tribol. Int.* **1999**, *32*, 469–480, doi:10.1016/S0301-679X(99)00077-8.
24. Lei, Y.; Lin, J.; He, Z.; Zuo, M.J. A Review on Empirical Mode Decomposition in Fault Diagnosis of Rotating Machinery. *Mech. Syst. Signal Process.* **2013**, *35*, 108–126, doi:10.1016/j.ymssp.2012.09.015.
25. Liu, X.; Han, F.; Wang, J. Wavelet Extended EMD Noise Reduction Model for Signal Trend Extraction. In Proceedings of the 2009 2nd International Congress on Image and Signal Processing; IEEE, October **2009**; pp. 1–5.
26. Kopsinis, Y.; McLaughlin, S. Development of EMD-Based Denoising Methods Inspired by Wavelet Thresholding. *IEEE Transactions on Signal Processing* **2009**, *57*, 1351–1362, doi:10.1109/TSP.2009.2013885.
27. Kumbhar, S.G.; Sudhagar P, E.; Desavale, R. An Overview of Dynamic Modeling of Rolling-Element Bearings. *Noise & Vibration Worldwide* **2021**, *52*, 3–18, doi:10.1177/0957456520948279.
28. Chen, H.; Fu, C.; Zhao, H.; Lu, K.; Zhang, Y. Stochastic Nonlinear Dynamics Analysis of Ball Bearings with Defects. *Nonlinear Dyn.* **2026**, *114*, 61, doi:10.1007/s11071-025-11909-3.
29. A²B Automotive Audio Bus Technology. Available online: https://www.analog.com/En/Solutions/A2b-Automotive-Audio-Bus.html (accessed on 31/03/**2026**).
30. Toscani, A.; Rocchi, N.; Pinardi, D.; Binelli, M.; Saccenti, L.; Farina, A.; Pavoni, S.; Vanali, M. Low-Cost Structural Health Monitoring System for Smart Buildings. In Proceedings of the 2022 Second International Conference on Sustainable Mobility Applications, Renewables and Technology (SMART); IEEE, November 23 **2022**; pp. 1–7.
31. Toscani, A.; Rocchi, N.; Pinardi, D.; Binelli, M.; Saccenti, L.; Farina, A.; Pavoni, S.; Vanali, M. Low-Cost Condition Monitoring System for Smart Buildings and Industrial Applications. *IEEE Trans. Ind. Appl.* **2024**, *60*, 1870–1878, doi:10.1109/TIA.2023.3326784.
32. Toscani, A.; Immovilli, F.; Pinardi, D.; Cattani, L. A Novel Scalable Digital Data Acquisition System for Industrial Condition Monitoring. *IEEE Transactions on Industrial Electronics* **2024**, *71*, 7975–7985, doi:10.1109/TIE.2023.3301521.
33. Pinardi, D.; Toscani, A.; Binelli, M.; Saccenti, L.; Farina, A.; Cattani, L. Full-Digital Microphone Meta-Arrays for Consumer Electronics. *IEEE Transactions on Consumer Electronics* **2023**, *69*, 640–648, doi:10.1109/TCE.2023.3267836.
34. Rocchi, N.; Toscani, A.; Pinardi, D.; Binelli, M.; Chiesi, L.; Farina, A.; Bonomi, E.; Tronchin, L. A Modular, Low Latency, A ² B-Based Architecture for Distributed Multichannel Full-Digital Audio Systems. In Proceedings of the 2021 Immersive and 3D Audio: from Architecture to Automotive (I3DA); IEEE, September 8 **2021**; pp. 1–8.
35. Rocchi, N.; Toscani, A.; Chiorboli, G.; Pinardi, D.; Binelli, M.; Farina, A. Transducer Arrays Over A²B Networks in Industrial and Automotive Applications: Clock Propagation Measurements. *IEEE Access* **2021**, *9*, 118232–118241, doi:10.1109/ACCESS.2021.3106710.
36. Antoni, J.; Randall, R.B. The Spectral Kurtosis: Application to the Vibratory Surveillance and Diagnostics of Rotating Machines. *Mech. Syst. Signal Process.* **2006**, *20*, 308–331, doi:10.1016/j.ymssp.2004.09.002.
37. Antoni, J. The Spectral Kurtosis: A Useful Tool for Characterising Non-Stationary Signals. *Mech. Syst. Signal Process.* **2006**, *20*, 282–307, doi:10.1016/j.ymssp.2004.09.001.